Figure 1

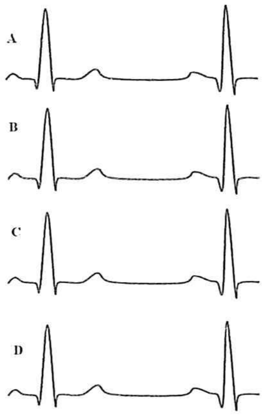

Figure 2

Figure 3

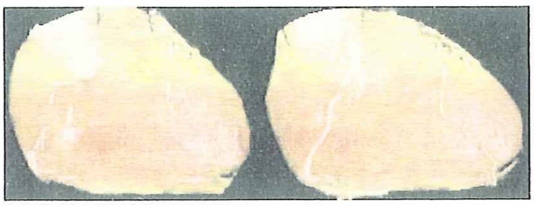

Figure 4A

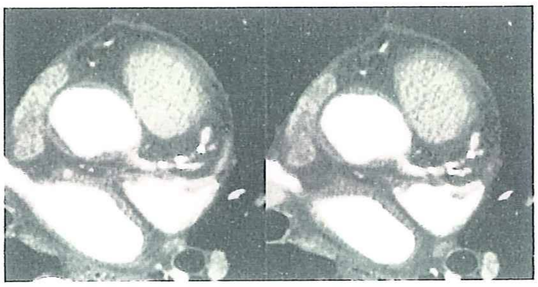

Figure 4B

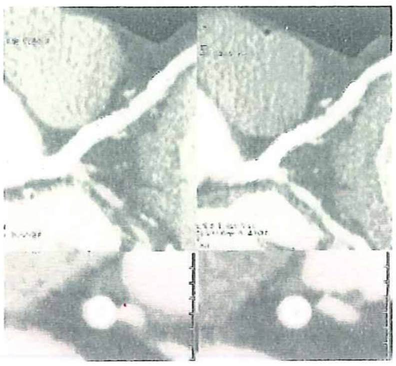

Figure 5

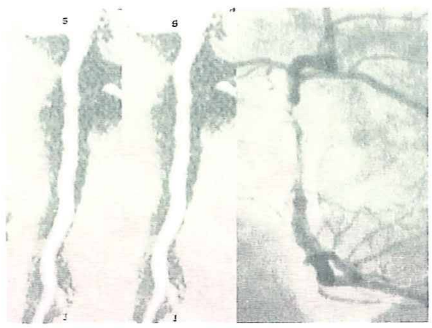

Circ J 2009; **73:** 691–698

Diagnostic Accuracy of Angiographic View Image for the Detection of Coronary Artery Stenoses by 64-Detector Row CT

— A Pilot Study Comparison With Conventional Post-Processing Methods and Axial Images Alone —

Masahiro Jinzaki, MD; Kozo Sato, MD; Yutaka Tanami, MD; Minoru Yamada, MS*; Toshihisa Anzai, MD**; Akio Kawamura, MD**; Koji Ueno, MD**; Sachio Kuribayashi, MD

Background: The angiographic view (AGV) image is a new post-processing method that is similar to conventional coronary angiography (CAG). The purpose of this study was to evaluate its accuracy for coronary stenosis detection by 64-detector row computed tomography (CT).

Methods and Results: CT evaluation results of 17 patients were compared with the results of invasive CAG on a coronary segment basis concerning the presence of stenoses >50% diameter reduction. All images of the 3 viewing methods (combination of conventional methods, AGV image alone, and axial images alone) were evaluated in consensus by 3 cardiovascular radiologists. Among 196 assessable segments, invasive CAG showed significant coronary artery stenoses in 44 segments. 43 of 44 lesions were detected with the AGV image, and absence of significant stenosis was correctly identified in 135 of 152 segments (sensitivity 98%; specificity 89%; accuracy 91%; positive predictive value 72%, negative predictive value 99%). The sensitivity of the AGV image was the same as that of conventional methods (98%). There was no significant difference in accuracy between the AGV image (91%) and conventional methods (94%). The accuracy of the AGV image was significantly higher than the axial images alone (78%).

Conclusions: AGV image shows promise as a post-processing method for identifying coronary artery stenosis with high accuracy. (*Circ J* 2009; **73:** 691–698)

Key Words: Computed tomography; Coronary angiography; Coronary artery disease; Maximum-intensity projection; Post-processing

Recent advances in multidetector-row computed tomography (MDCT) have enabled non-invasive evaluation of coronary artery stenoses with high accuracy.[1–4] Diagnostic evaluation of coronary artery stenoses includes review of the originally reconstructed axial images, as well as various post-processing images. The important role of post-processing images is to integrate the series of axial CT sections into a form that is easier to interpret and the axial images can be made to appear similar to other, more familiar images such as those from invasive angiography.[5–9] In these aspects, current methods, such as volume rendering (VR), partial maximum intensity projection (partial MIP), curved multiplanar reconstruction (curved MPR), or cross-sectional images, fall short. VR enables overview of the coronary artery to third parties, but it is not usually used for the evaluation of coronary artery stenoses. For coronary artery stenoses, partial MIP, curved MPR or cross-sectional images are used, but these conventional methods are quite different from the images obtained with invasive coronary angiography (CAG), and it can be difficult for a third person to understand which artery or segment is being analyzed.

The angiographic view (AGV) image is a MIP image in which contrast media in the ventricles is eliminated.[7] This image is similar to that from invasive CAG and thus familiar to cardiologists. This type of MIP image clearly demonstrates the distribution of high-density lesions, such as coronary calcifications and stents, in the 1 image. If coronary artery stenoses can also be identified on the AGV image with high accuracy, it will be the post-processing method with most promise for accurately showing the distribution of coronary lesions that is understandable by third parties such as referral physicians and the patients.

In this study, we evaluated the accuracy of the AGV image in comparison with axial images alone and a combination of conventional methods for coronary stenoses detection.

(Received August 18, 2008; revised manuscript received November 21, 2008; accepted December 7, 2008; released online February 18, 2009)
*Department of Diagnostic Radiology, *Division of Cardiovascular Imaging Laboratory, Research Park and **Division of Cardiology, Department of Medicine, Keio University School of Medicine, Tokyo, Japan*
Mailing address: Masahiro Jinzaki, MD, Department of Diagnostic Radiology, Keio University School of Medicine, 35 Shinanomachi, Shinjuku-ku, Tokyo 160-8582, Japan. E-mail: jinzaki@sc.itc.keio.ac.jp

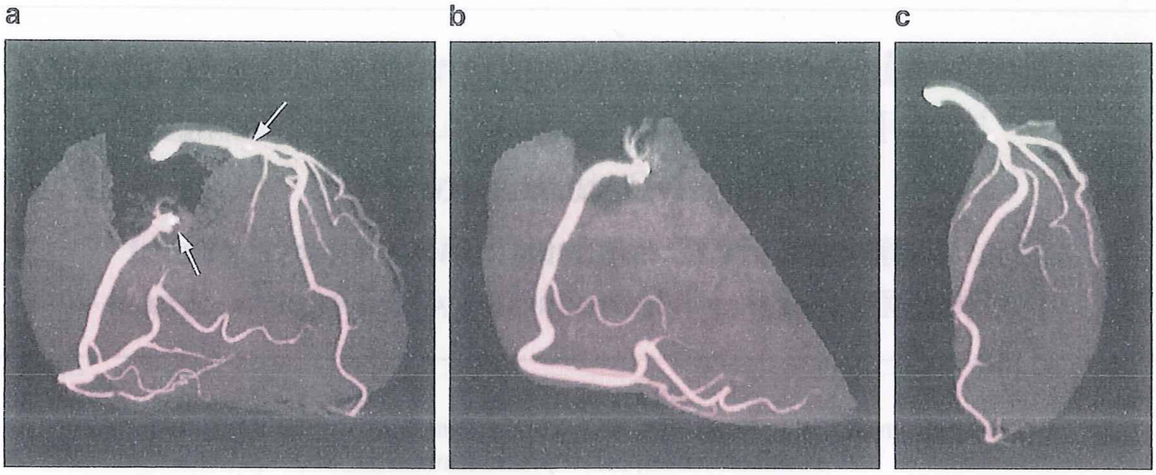

Figure 1. Angiographic view (AGV) of the coronary arteries (a) enables an overview of the coronary tree. The AGV is divided into right (b) and left (c) coronary artery, and viewed from various angles. The distribution of calcifications (arrows) is shown.

Table 1. Diagnostic Accuracy of Each Viewing Method: Test Characteristics by Segments

	Sensitivity	Specificity	PPV n/total n (%)	NPV	Accuracy
Angiographic view image	43/44 (98)	135/152 (89)	43/60 (72)	135/136 (99)	178/196 (91)
Conventional methods	43/44 (98)	141/152 (93)	43/54 (80)	141/142 (99)	184/196 (94)
Axial images alone	38/44 (86)	115/152 (76)	38/75 (51)	115/121 (95)	153/196 (78*)

*P<0.05 for angiographic view vs axial images alone and conventional methods vs axial images alone.
PPV, positive predictive value; NPV, negative predictive value.

Methods

Patient databases from the Catheter Angiography Laboratory and Radiology Department were reviewed for patients who had undergone both invasive CAG and CT CAG within 1 month and without other interventions in the meantime. We identified 18 consecutive patients from May 2005 to September 2005, but 1 was excluded because of atrial fibrillation. Thus, data of 17 patients (15 men, 2 women; 35–80 years, average 58 years) were available. The average heart rate (HR) of these patients was 58.6±6.6 beats/min (44–72 beats/min; 16 patients with HR <70 beats/min, 1 patient with HR >70 beats/min). Retrospective evaluation of patient data acquired during clinical routines is approved by the Institutional Review Board, and written informed consent was not obtained from the patients.

MDCT Data Acquisition

Computed tomography (CT) CAG was performed using 64-detector row CT (LightSpeed VCT: GE Healthcare, Milwaukee, WI, USA). Nitroglycerin spray (0.3 mg, glycerol trinitrate) was administered sublingually immediately before the scan; β-blocker was not administered prior to the scan. The delay between the start of injection and scanning was determined by the test bolus technique, monitoring at the level of the ascending aorta. The dynamic monitoring scans started 10 s after beginning the injection of intravenous contrast material (10 ml of contrast material followed by 15 ml of saline injected at 4 ml/s), and were obtained every 2 s with low-dose (120 kV, 20 mA).The delay applied for the main scanning was calculated by the time to peak enhancement for the test bolus plus 2 s. The main scanning was performed with 64×0.625 mm collimation, acquiring the entire heart within 5 to 6s. The gantry rotation time was 0.35s, and the pitch was between 0.20 and 0.22. The tube current was 350–550 mA at 120 kV. Iodine contrast material (40–60 ml; Iopamidol 370 mgI/ml) was immediately followed by 20 ml of saline, injected at a rate of 4 ml/s. The estimated effective radiation dose was 15–19 mSv. ECG-gated datasets were reconstructed automatically at 75% of the R-R interval and 45% of the R-R interval to create a stack of contiguous axial images with a section thickness of 0.625 mm and an increment of 0.625 mm. Depending on the HR, 2 reconstruction algorithms were applied: a single-segmental reconstruction (<70 beats/min) and multisector (2 or 4) reconstruction (>70 beats/min). If motion artifacts were present in any coronary artery, image reconstruction was repeated with the reconstruction window offset by 5% toward the beginning or end of the cardiac cycle, and multiple reconstructions were obtained until all arteries were depicted free of motion artifact or until reconstructions in 5% intervals throughout the cardiac cycle had been obtained.

Invasive CAG

Invasive CAG was performed by experienced cardiologists using standard techniques and the acquisition of standard projection planes. Stenosis severity was determined by quantitative CAG (QCA) (QuantCor.QCA,Pie Medical Imaging, Maastricht, The Netherlands). The grade of diameter stenosis (maximum diameter reduction) was determined by dividing the minimal diameter in the diseased segment by the diameter in the adjacent proximal disease-free section.

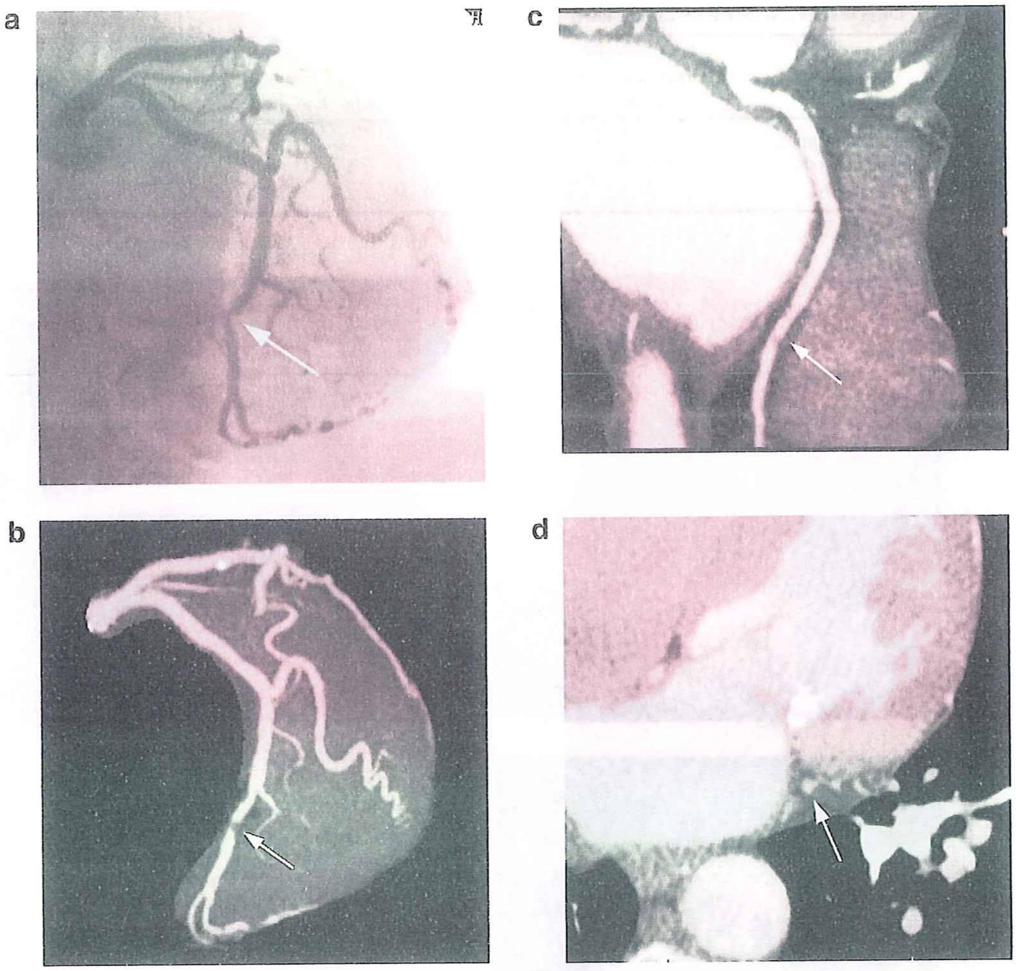

Figure 2. A 67-year-old woman with a significant stenosis in the distal left circumflex artery on the invasive angiogram (**a**: arrow). This lesion was correctly diagnosed as >50% stenoses with all viewing methods: angiographic view image (**b**: arrow), conventional methods (**c**: arrow), and axial images (**d**: arrow).

MDCT Image Analysis

CT axial images were transferred to a standard commercial workstation (GE Advantage Workstation 4.3) where the AGV image was automatically created as follows.

(1) The whole heart is extracted from the 3D volume data, after cutting and removing unnecessary regions such as bone, aorta and liver.

(2) Contrast medium within the endocardium is identified as ventricular.

(3) The ventricular area is subtracted from the whole heart image.

(4) MIP display of the image shows the coronary artery network identical to that seen with invasive CAG.

The AGV image can be spun around and viewed in various angles. Similar images can be created by tracking and extracting the coronary artery itself. However, tracking or extracting requires the threshold of CT attenuation, so the images can vary depending on the threshold, and the ability of the workstation used. The AGV image keeps the coronary artery untouched, and thus the image does not vary among workstations.

One technologist (4 years experience in cardiac CT imaging) who was unaware of the results of conventional CAG rendered curved MPR and AGV images. Curved MPRs were rendered with 0.6-mm section thickness, displaying all 15 segments of the AHA model in 2 orientations (with longitudinal and cross-sectional images as reference). Whether each coronary segment seen on the axial images was also identified by the conventional methods and on the AGV image was checked by this blinded technologist. The data sets were then stored for further analysis.

All images for the 3 viewing methods (ie, combination of conventional methods [axial images, partial MIP, partial MPR, and curved MPR], AGV image alone, and axial images alone) were evaluated in consensus by 3 cardiovascular radiologists: 2 with 5 years experience and 1 with 4 years experience in CT CAG. The readers were unaware of the patient's history, clinical details and QCA findings. First, the conventional methods were assessed, then the AGV image alone, and lastly the axial images alone, all at 2-week intervals. In the reading of the conventional methods, the readers interactively rendered partial MPRs or partial MIPs by using a 0.6-mm-thickness, and comprehensively reviewed these images, the axial images, and curved MPRs on the workstation. Axial images and curved MPRs were initially displayed with a default window setting (level, 100HU; window, 700HU). The AGV image was divided into the right and left coronary artery, similar to images from invasive CAG, and the readers viewed various angles of the images (**Figure 1**). The AGV image was initially dis-

Table 2. Location of False-Negative Lesions of Each Viewing Method

	Vessel branching out from mid-portion of the stent	Lesion located in the just proximal portion of the branch	Lesion located at the segment running horizontal to the axial section	Total
Angiographic view image	1	0	0	1
Conventional methods	0	1	0	1
Axial images alone	1	0	5	6

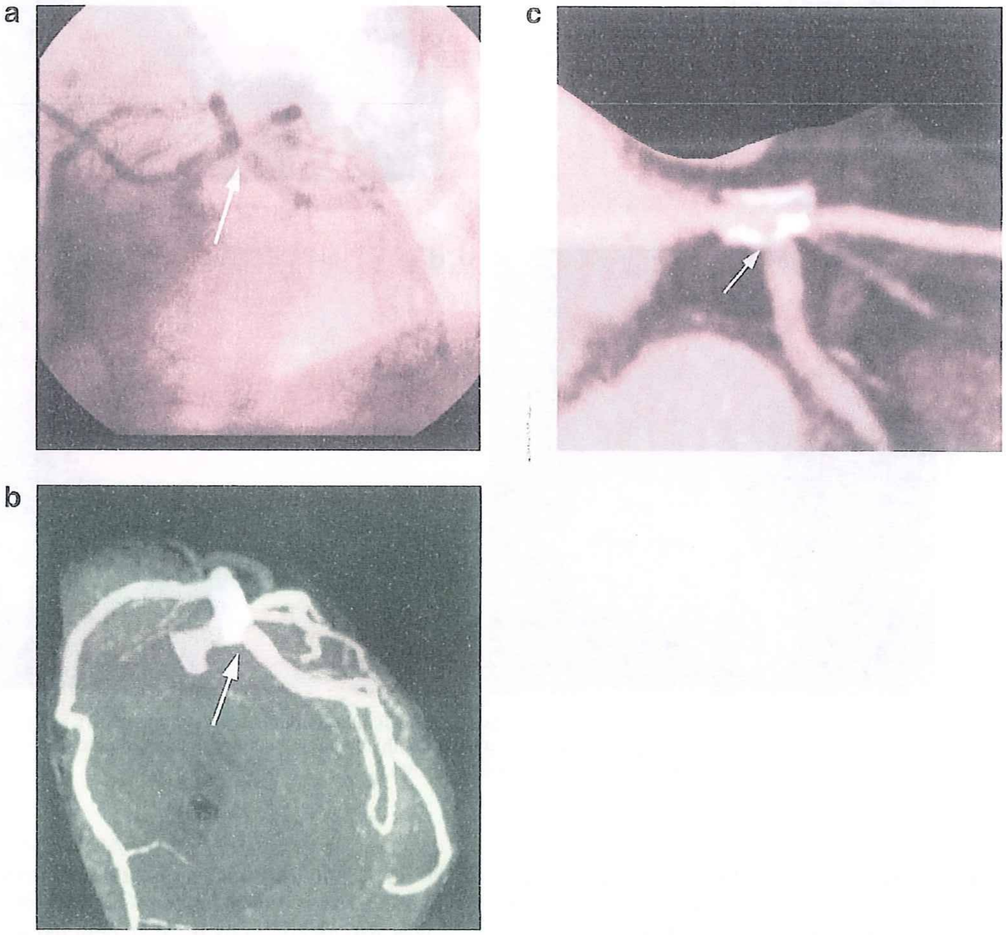

Figure 3. A 55-year-old man with a significant stenosis in the just proximal portion of the left circumflex artery on the invasive angiogram (**a**: arrow). This lesion was not detected (false negative) on the angiographic view image (**b**: arrow), but was correctly diagnosed as >50% stenosis by the conventional methods (**c**: arrow) and on the axial images (not shown).

played with a default window setting (level, 350HU; window, 700HU). The window and level of the evaluated images was then adjusted by the observer. Segments with severe calcifications (occupying more than half the circumference), stents, a vessel caliber less than 1.5 mm as defined on conventional CAG, or with a discontinuous area because of premature beat were excluded from the analysis.

All analyses were performed on a coronary segment basis (15 segments of the AHA model). Each segment was categorized by the presence or absence of a stenoses of 50% diameter reduction or more. MDCT evaluation results were documented in writing and then compared with the results of QCA. True positives were defined as correct identification by MDCT of segments of more than 50% diameter and true negatives were defined as correct identification by MDCT of segments of 50% or less. Segments that had inconsistencies between QCA and each viewing method were retrospectively re-evaluated by the 3 radiologists.

Statistical Analysis

The sensitivity, specificity, positive predictive value (PPV), and negative predictive value (NPV) of each of the viewing methods for detection of hemodynamically significant stenoses (≥50%) as compared with the reference standard (QCA) were calculated for each segment. We compared the accuracy of the different viewing methods for the detection of stenoses using McNemar's test. Statistical significance was considered to be present at $P<0.05$. Statistical analysis was performed using SPSS (version 13.0; SPSS, Chicago, IL, USA).

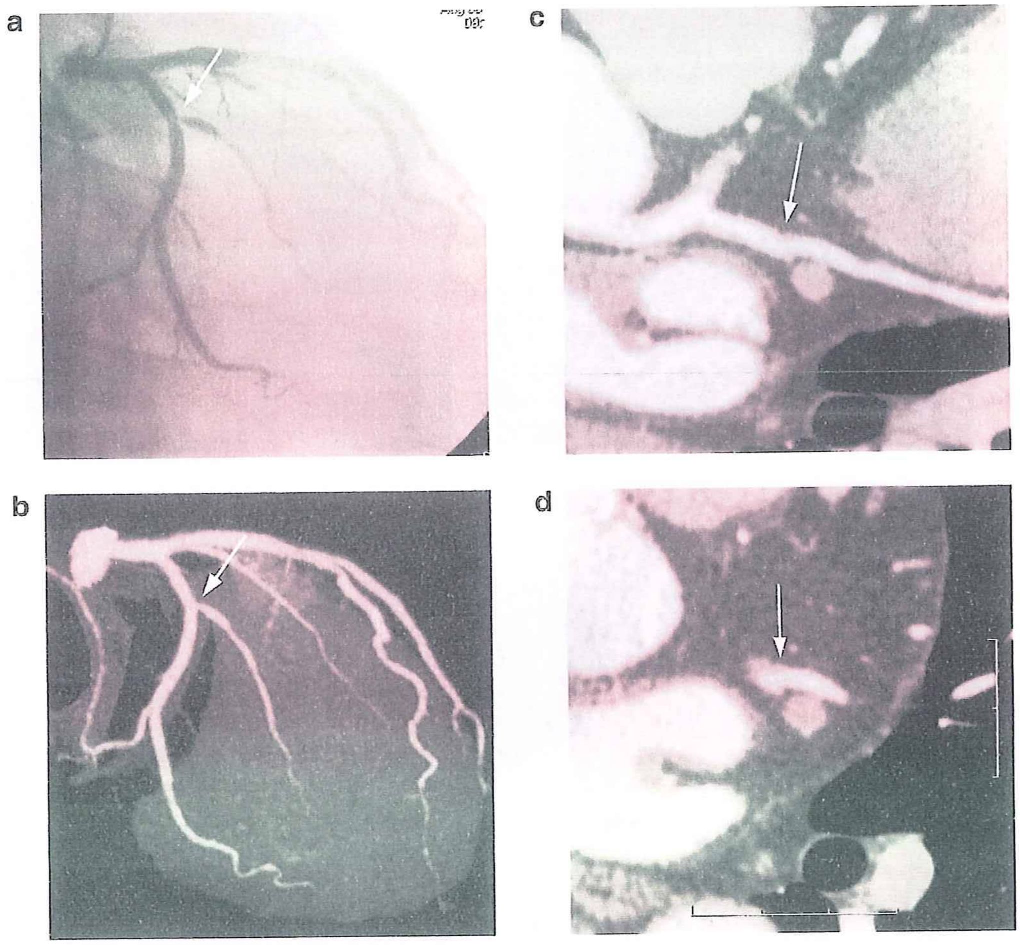

Figure 4. A 63-year-old man with a significant stenosis located in the just proximal portion of the obtuse marginal branch on the invasive angiogram (**a**: arrow). This lesion was diagnosed as >50% stenosis on the angiographic view image (**b**: arrow), but was judged to be <50% stenoses (false negative) with the conventional methods (**c**: arrow) and on the axial images (**d**: arrow).

Table 3. Results of Quantitative Coronary Angiography for False-Positive Lesions of Each Viewing Method

	Lesions with no severe calcification			Lesions with severe calcification			Total
	Mild stenosis	Trivial stenosis	No stenosis	Mild stenosis	Trivial stenosis	No stenosis	
Angiographic view image	7	1	1†	5	3	0	17
Conventional methods	3	1	0	4	3	0	11
Axial images alone	25	1	4	4	3	0	37

Mild stenosis: 26–50%; trivial stenosis: 1–25% stenoses.
†Muscular bridge.

Results

Of 208 segments >1.5 mm in diameter, 196 segments were included. Among the 12 segments excluded, 10 had stents and 2 were segments with a discontinuous area because of premature beat. QCA showed significant coronary artery stenoses (ie, 1 or more stenoses >50%) in 22% (44/196) of the segments. All coronary segments >1.5 mm in diameter and seen on the axial images were also identified by the conventional methods and on the AGV image.

Diagnostic Accuracy of Each Viewing Method

Table 1 shows the results of the 3 viewing methods for lesion detection by coronary artery segment. In the comparison of the AGV image and conventional methods, sensitivity was the same (98%) and there was no significant difference in accuracy (P>0.05: 91% with AGV image and 94% with conventional methods) (**Figure 2**). The accuracy of the AGV image was significantly higher compared with axial images alone (P<0.05).

False-Negative (FN) Lesions of Each Viewing Method

The location of the FN lesion differed among the viewing methods (**Table 2**).

With the AGV image, a FN lesion was located just proximal portion to the left circumflex artery where the vessel

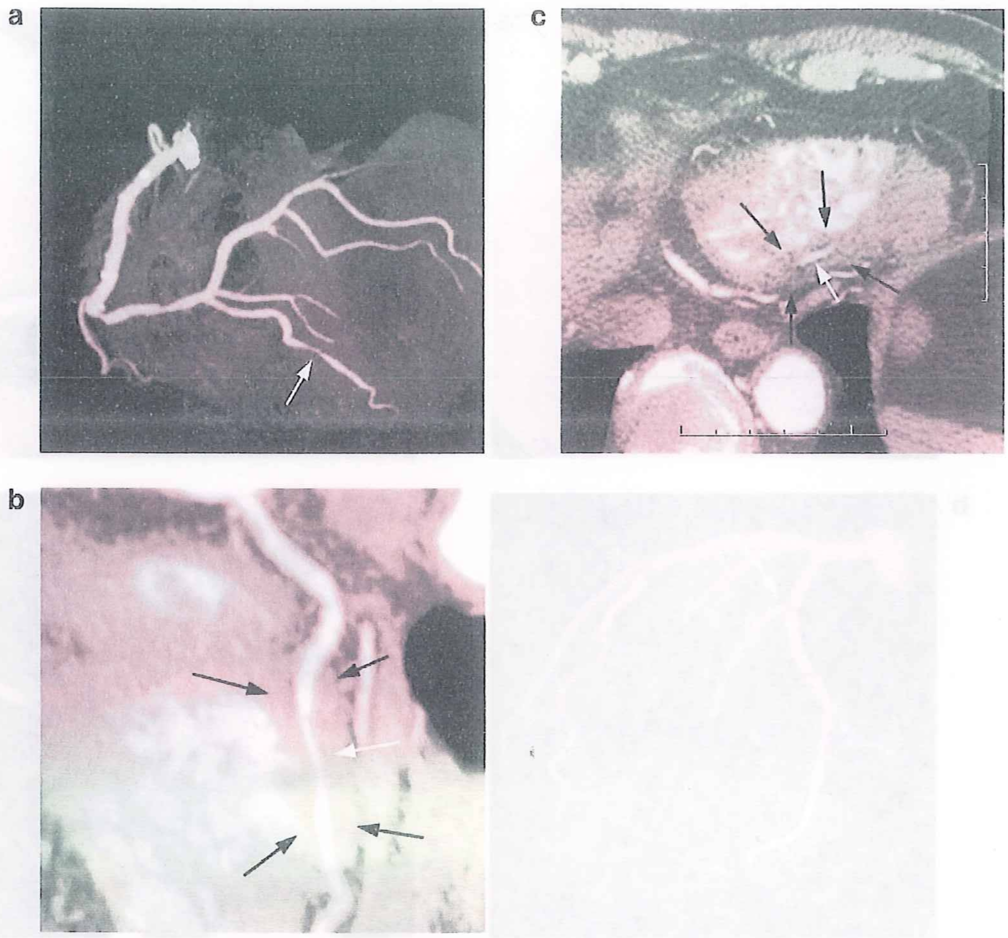

Figure 5. A 73-year-old man with a myocardial bridge in the poster descending branch. The lesion was judged as >50% stenosis on the angiographic view (**a**: arrow). With the conventional methods (**b**) and on the axial images (**c**), this lesion (white arrow) seemed to be >50% stenosis, but was judged to be a myocardial bridge not a stenotic lesion because of plaque, because myocardium (black arrows) was seen surrounding the lesion.

branched out from the mid-portion of the stent (**Figure 3**). This may have been a stent artifact, which appears to "bloom" the outer margin of the stent, hiding lesions in the just proximal portion from view.

With the conventional methods, a FN lesion was located in the just proximal portion of the obtuse marginal artery (**Figure 4**). This type of lesion can appear stenotic using projection methods such as the AG view and QCA, but as seen with the conventional methods, it may in fact be non-stenotic. However, if QCA is used as the gold standard, the result will be an AGV image true-positive and conventional false-negative.

With the axial images alone, 5 of 6 FN lesions were located in the segment running horizontal to the axial section, and the remaining 1 was the same as the FN lesion in the AGV image.

False-Positive (FP) Lesions of Each Viewing Method

The FP lesions for each viewing method varied with the results of QCA (**Table 3**). The FP lesions were divided into 2 categories: with and without severe calcification.

Lesions With Severe Calcification The total number of lesions with severe calcification was 24. On the AGV image, 5 of the 8 FP lesions with severe calcification were mild stenoses (26–50%), and 3 were trivial (1–25%). With the conventional methods and on the axial images alone, 4 of 7 FP lesions were mild stenoses and 3 were trivial stenoses. The "blooming" artifact of calcification was considered to cause the overestimation of mild or trivial stenoses. One severe calcification of a mild stenosis was FP only on the AGV image, and true-positive with the conventional methods and the axial images alone.

Lesions With No Severe Calcification The total number of lesions with no severe calcification was 172. On the AGV image, 7 of the 9 FP lesions with no severe calcification were mild stenoses, 1 was a trivial stenosis, and the other was a non-stenosis on QCA. Thus, the main cause of FP lesions on the AGV image was overestimation of mild stenoses as >50% stenoses. One trivial-stenotic lesion was accompanied by protruding moderate calcification (occupying less than 50% diameter), thus the blooming artifact of calcification was considered to cause the overestimation of trivial stenoses as >50% stenoses on the AGV image. One non-stenotic lesion on QCA was a myocardial bridge (**Figure 5**). This lesion was also viewed as stenotic by the conventional methods and on the axial images alone. However, those methods demonstrated the myocardium surrounding the vessel, and thus enabled the correct diagnosis of myocardial bridge not stenotic lesion because of plaque.

With the conventional methods, 3 of the 4 FP lesions were mild stenoses on QCA, and the other was a trivial stenosis (same as with the FP lesion on the AGV image ; the lesion was accompanied by protruding moderate calcification).

On the axial images alone, 25 of the 30 FP lesions were mild stenoses, 1 was a trivial stenosis, and 4 were non-stenoses on QCA. The number (n=30) of FP was much more than on the AGV images (n=9) or with the conventional methods (n=4). This was retrospectively considered to be related to evaluation of lesions located in the segment running horizontal to the axial section, and that diffuse concentric plaque with positive remodeling in all length of segment is more difficult to determine on axial images compared with other methods. Among the 30 FP lesions on the axial images alone, 14 were located in the segment running horizontal to the axial section (horizontal lesion), and 4 were diffuse concentric plaque with positive remodeling in all length of segment (concentric lesion). Among the 9 FP lesions on the AGV images, only 1 was a horizontal lesion and 0 with the conventional methods, and no concentric lesions with either method.

Discussion

The axial image is the basic clinical reference for detailed image analysis. However, because of the complex course of the coronary artery, interpretation of axial images may be difficult and the use of post-processing techniques enables investigators to better understand the complex coronary artery anatomy and abnormalities. There have been several studies of the use of various post-processing methods for CT CAG and according to their results, a combination of various viewing methods gives the highest sensitivity, and was used in most of the studies.[10–12] Thus, we compared the diagnostic accuracy of the AGV image with a combination of various viewing methods, and also with axial images alone.

We found significant coronary artery stenoses were detected on the AGV image with a sensitivity of 98% and specificity of 89%, and with 98% and 93%, respectively, by the conventional methods. Our findings are comparable with those from recent reports of the accuracy of 64-slice CT for the detection of coronary artery stenoses (sensitivity: 93–99%, specificity: 86–97% and NPV 98–99%) analyzed by a combination of conventional methods.[2–4,13–15] In the present study, there was only 1 FN finding on the AGV image, which was a very rare lesion located in the just proximal portion of the left circumflex artery where the vessel branches out from the mid-portion of the stent, and the sensitivity of the AGV image was the same as that with the conventional methods. Our results show that the AGV image is a reliable method of identifying significant stenoses.

The accuracy of the AGV image, as with the conventional methods, was significantly higher compared with the axial images alone. Correct diagnosis was more difficult with the axial images than the other viewing methods in the lesions located in the segment running horizontal to the axial section. Diffuse concentric plaque with positive remodeling also has a tendency to be incorrectly viewed as stenotic on axial images, possibly because the reference diameter (vessel diameter in non-diseased artery immediately proximal to the lesion) of these lesions is not measurable on the axial image. For evaluation of these types of lesions, the post-processing image is better suited, although this is a pilot study and thus will require further evaluation. In a previous study, the sensitivity of the axial image (73.4%) was reported to be superior to virtual angioscopic (49.1%), VR (43.0%), and MPR images (46.8%) from 4-section multidetector CT.[8] It seems that axial images are less susceptible to motion artifacts, and the poor results obtained for MPR may have been because strictly orthogonal reformation were obtained only along the centerline of virtual endoscope images and, consequently, segments not captured with VE were also not displayed on the MPRs.[16] The 64-detector row CT decreased the frequency of motion artifact, and because the post-processing image can be created in any angle without restrictions, a higher diagnostic accuracy can be expected than with axial images. Another recent study reported high diagnostic accuracy of axial images (sensitivity of 89% and specificity of 89% in assessable arteries and an overall accuracy of 88%) using 16-section multidetector CT.[16] This high accuracy may be related to per-artery analysis, not per-segment analysis as in our study, and exclusion of side branches from analysis.

The AGV image is a noninvasive overview of all the coronary arteries and accurately shows the distribution of coronary stenoses in 1 set of images that is understandable by third parties. This would be useful in several situations. First, it would be useful for explaining the severity of disease to the patient. Second, the AGV image can be divided into right and left coronary artery, resembling the images from invasive CAG, which enables viewing the lesions from the same angle as with QCA, and detecting the best angle of the lesion prior to percutaneous coronary intervention would be useful in the discussion of the treatment strategy in conference.

The major drawback of the AGV image is that the specificity for coronary stenosis detection compared with conventional methods was lower, the main cause being overestimation of mild stenoses on QCA as >50% stenoses on the AGV image. Previous studies report that MIP can overestimate the degree of stenosis,[17–21] so because the AGV image is a MIP image, the lower specificity is understandable. However, this drawback is considered not to be a problem, because the most important factor for the identification of stenotic lesions is high sensitivity.

It is usually difficult to accurately assess the degree of stenosis of lesions with severe calcification.[1–4] In our study, 8 of 24 (33%) lesions with severe calcification were FP on the AGV image, and 7 of 24 (29%) lesions were FP with the conventional methods and on the axial images alone. Further study in a larger number is necessary to clarify the characteristics of each viewing method for the evaluation of lesions with severe calcification.

Study Limitations

First, this was a pilot study and thus the number of subjects was small. Second, QCA was used as the gold standard, but it has its imperfections; stenotic lesions may be missed.

Conclusion

The AGV image shows promise as a reliable post-processing method of identifying coronary artery stenoses. Because the AGV image demonstrates coronary lesions in the 1 image, it would be useful for explaining the severity of disease to the patient, and for discussing the treatment strategy in conference.

References

1. Ropers D, Baum U, Pohle K, Anders K, Ulzheimer S, Ohnesorge B, et al. Detection of coronary artery stenoses with thin-slice multi-detector row spiral computed tomography and multiplanar reconstruction. *Circulation* 2003; **107:** 664–666.
2. Raff GL, Gallagher MJ, O'Neill WW, Goldstein JA. Diagnostic accuracy of noninvasive coronary angiography using 64-slice spiral computed tomography. *J Am Coll Cardiol* 2005; **46:** 552–557.
3. Mollet NR, Cademartiri F, van Mieghem CA, Runza G, McFadden EP, Baks T, et al. High-resolution spiral computed tomography coronary angiography in patients referred for diagnostic conventional coronary angiography. *Circulation* 2005; **112:** 2318–2323.
4. Goldstein JA, Gallagher MJ, O'Neill WW, Ross MA, O'Neil BJ, Raff GL. A randomized controlled trial of multi-slice coronary computed tomography for evaluation of acute chest pain. *J Am Coll Cardiol* 2007; **49:** 863–871.
5. Calhoun PS, Kuszyk BS, Heath DG, Carley JC, Fishman EK. Three-dimensional volume rendering of spiral CT data: Theory and method. *Radiographics* 1999; **19:** 745–764.
6. Feyter PJ, Krestin GP. Image post-processing. *In*: Feyter PJ, Krestin GP, editors. Computed tomography of the coronary arteries. New York: Taylor & Francis; 2005; 27–46.
7. Jinzaki M, Sato K, Tanami Y, Yamada M, Kuribayashi S, Anzai T, et al. Novel method of displaying coronary CT angiography: Angiographic view. *Circ J* 2006; **70:** 1661–1662.
8. Jinzaki M, Yamada M, Sato K, Tanami Y, Anzai T, Sasaki K, et al. Overview image of the lumen and vessel wall in coronary CT angiography: Plaque-loaded angiographic view. *Circ J* 2008; **72:** 671–673.
9. Yamada M, Jinzaki M, Kuribayashi S, Sato K, Tanami Y, Fukumoto K, et al. Novel post-processing image for the visualization of coronary sinus by multidetector-row computed tomography before cardiac resynchronization therapy: Edge-enhanced image. *Circ J* 2008; **72:** 487–488.
10. Pannu HK, Flohr TG, Corl FM, Schoepf UJ. Current concepts in multidetector row CT evaluation of the coronary arteries: Principles, techniques, and anatomy. *Radiographics* 2003; **23:** S111–S125.
11. Ferencik M, Ropers D, Abbara S, Cury RC, Hoffmann U, Nieman K, et al. Diagnostic accuracy of image postprocessing methods for the detection of coronary artery stenoses by using multidetector CT. *Radiology* 2007; **243:** 696–702.
12. Pugliese F, Mollet NR, Runza G, van Mieghem C, Meijboom WB, Malagutti P, et al. Diagnostic accuracy of non-invasive 64-slice CT coronary angiography in patients with stable angina pectoris. *Eur Radiol* 2006; **16:** 575–582.
13. Ropers D, Rixe J, Anders K, Küttner A, Baum U, Bautz W, et al. Usefulness of multidetector row spiral computed tomography with 64-×0.6-mm collimation and 330-ms rotation for the noninvasive detection of significant coronary artery stenoses. *Am J Cardiol* 2006; **97:** 343–348.
14. Vanhoenacker PK, Heijenbrok-Kal MH, Van Heste R, Decramer I, Van Hoe LR, Wijns W, et al. Diagnostic performance of multidetector CT angiography for assessment of coronary artery disease: Meta-analysis. *Radiology* 2007; **244:** 419–428.
15. Achenbach S, Moshage W, Ropers D, Bachmann K. Curved multiplanar reconstructions for the evaluation of contrast-enhanced electron beam CT of the coronary arteries. *Am J Roentgenol* 1998; **170:** 895–899.
16. Vogl TJ, Abolmaali ND, Diebold T, Engelmann K, Ay M, Dogan S, et al. Techniques for the detection of coronary atherosclerosis: Multidetector row CT coronary angiography. *Radiology* 2002; **223:** 212–220.
17. Lu B, Dai RP, Bai H, He S, Jing BL, Jiang SL, et al. Coronary artery stenoses: A phantom study using contrast enhanced three-dimensional electron beam tomography. *Clin Imaging* 2001; **25:** 95–100.
18. Uchino A, Kato A, Kudo S. CT angiography using electron-beam computed tomography (EBCT): A phantom study. *Radiat Med* 1997; **15:** 273–276.
19. Brink JA, Lim JT, Wang G, Heiken JP, Deyoe LA, Vannier MW. Technical optimization of spiral CT for depiction of renal artery stenosis: In vitro analysis. *Radiology* 1995; **194:** 157–163.
20. Dillon EH, van Leeuwen MS, Fernandez MA, Eikelboom BC, Mali WP. CT angiography: Application to the evaluation of carotid artery stenosis. *Radiology* 1993; **189:** 211–219.
21. Rubin GD, Dake MD, Napel S, Jeffrey RB Jr, McDonnell CH, Sommer FG, et al. Spiral CT of renal artery stenosis: Comparison of three-dimensional rendering techniques. *Radiology* 1994; **190:** 181–189.

JACC: CARDIOVASCULAR INTERVENTIONS
VOL. 2, NO. 12, 2009

ISSN 1936-8798/09/$36.00
PUBLISHED BY ELSEVIER INC.
DOI: 10.1016/j.jcin.2009.07.018

Progression of Late Stent Malapposition Beyond 2 Years After Sirolimus-Eluting Stent Implantation

Koji Ueno, MD,* Akio Kawamura, MD,* Gary S. Mintz, MD,‡ Neil J. Weissman, MD,§ Masahiro Jinzaki, MD,† Teruo Okabe, MD,* Naoshi Kobayakawa, MD,‖ Minoru Yamada, PhD,† Sachio Kuribayashi, MD,† Satoshi Ogawa, MD*

Tokyo, Japan; New York, New York; and Washington, DC

Recent reports suggest that late stent malapposition (LSM) might be associated with stent thrombosis.

We show a series of angiograms, intravascular ultrasound, and multidetector computed tomogra-

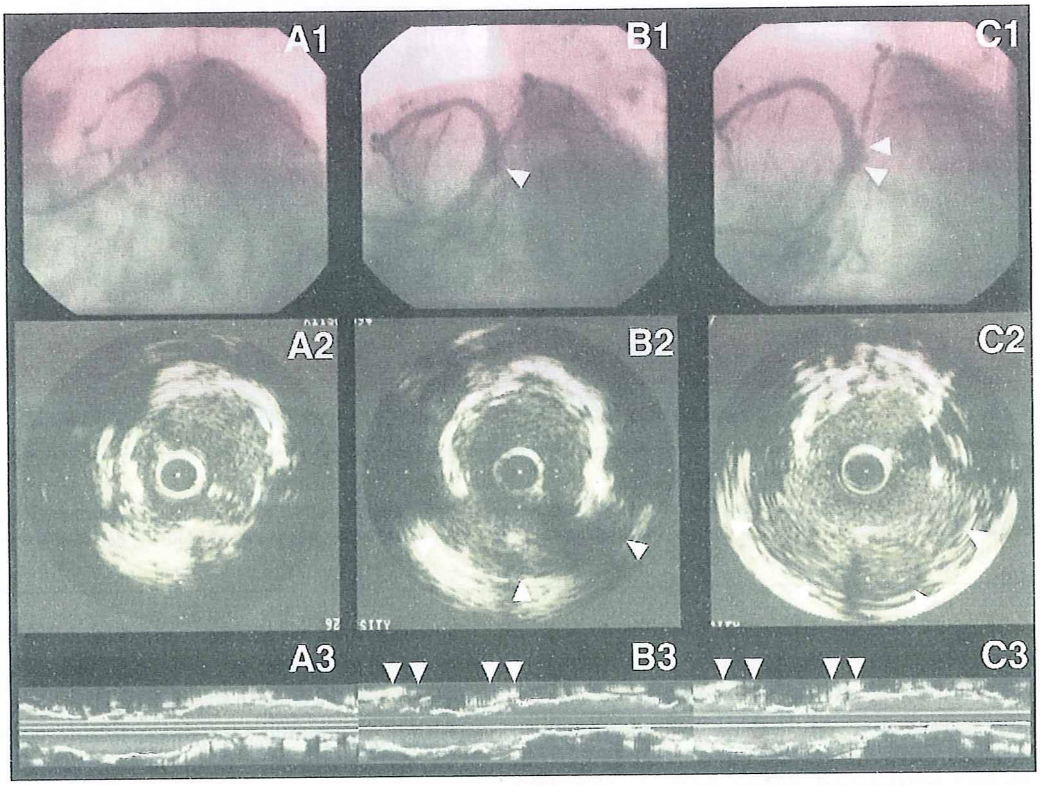

Figure 1. Coronary Angiograms and IVUS Images Showing Gradual Progression of LSM

(A1 to A3) Just after sirolimus-eluting stents implantation. Cross-sectional and longitudinal intravascular ultrasound (IVUS) images show well-apposed stents. **(B1 to B3)** At 10-month follow-up. Late stent malapposition (LSM) is confirmed at the proximal part of the stents **(arrowheads)**. **(C1 to C3)** After 30 months presenting with an acute coronary syndrome. Coronary angiogram shows further outward expansion of stented segment. Cross-sectional and longitudinal IVUS images show progressive large LSM due to positive vessel remodeling at the proximal part of the stents **(arrowheads)**.

From the *Division of Cardiology and the †Division of Diagnostic Radiology, Department of Medicine, Keio University School of Medicine, Tokyo, Japan; ‡Cardiovascular Research Foundation, New York, New York; §MedStar Research Institute, Washington Hospital Center, Washington DC; and the ‖Japanese Red Cross Medical Center, Tokyo, Japan.

Manuscript received July 6, 2009, accepted July 25, 2009.

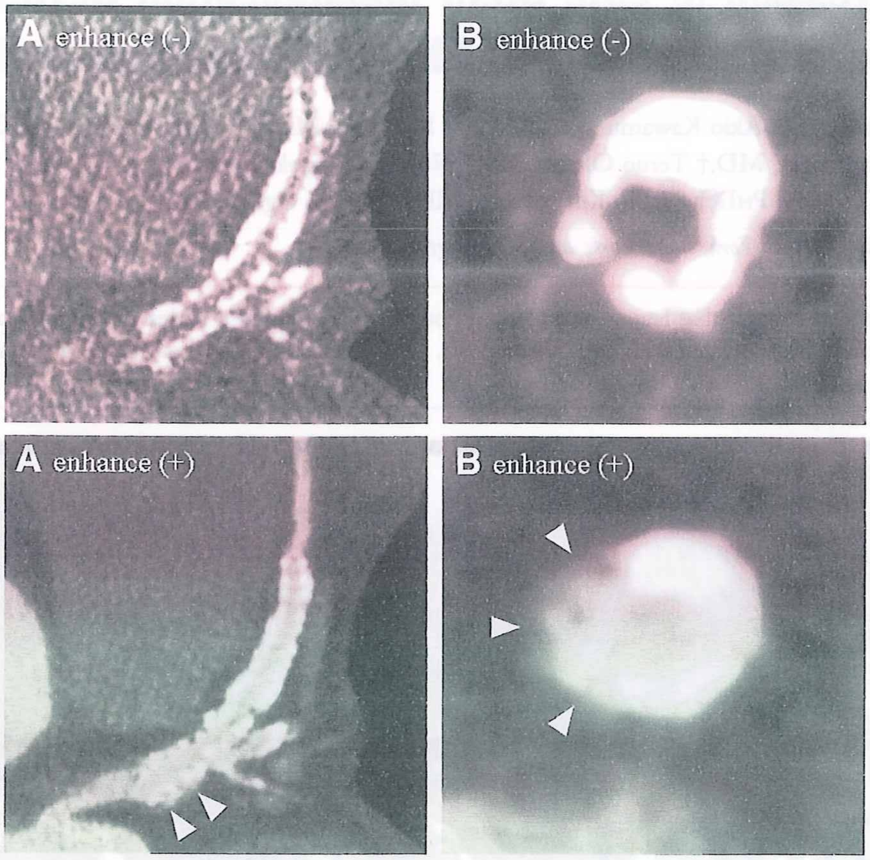

Figure 2. 64-MDCT Images Demonstrating LSM

(A) Curved multiplanar reformation. (B) Cross-sectional images. Multidetector computed tomography (MDCT) clearly visualizes late stent malapposition (LSM) as the high-density area (arrowheads) outside of the stents in enhanced images. We suggest that MDCT can be a useful tool for the detection and vigilant follow-up of large LSM.

phy images of LSM that continued to progress beyond 2 years and caused acute thrombotic events.

Two sirolimus-eluting stents were implanted in the proximal left descending artery (LAD) with good apposition in September 2005 (Figs. 1A1, 1A2, and 1A3). The LSM was evident at 10-month follow-up (Figs. 1B1, 1B2, and 1B3). Then LSM showed continuous progression and resulted in acute coronary syndrome 30 months later (Figs. 1C1, 1C2, 1C3, and 2). The patient was treated medically, including dual antiplatelet therapy. In March 2009 (42 months later), the patient was admitted for severe gastrointestinal bleeding. Unfortunately, he developed late stent thrombosis 2 weeks after the dual antiplatelet therapy was stopped. Emergency coronary angiography revealed a thrombotic occlusion of left main trunk and proximal LAD. Although percutaneous coronary intervention was successful, the patient died from multiorgan failure.

Reprint requests and correspondence: Dr. Akio Kawamura, Division of Cardiology, Department of Medicine, Keio University School of Medicine, 35 Shinanomachi, Shinjuku-ku, Tokyo 160-8582, Japan. E-mail: kawamura@cpnet.med.keio.ac.jp.

Computed Tomographic Attenuation Value of Coronary Atherosclerotic Plaques With Different Tube Voltage: An Ex Vivo Study

Yutaka Tanami, MD,† Eiji Ikeda, MD, PhD,*‡ Masahiro Jinzaki, MD, PhD,† Kozo Satoh, MD,† Yuji Nishiwaki, MD, PhD,§ Minoru Yamada, MS,|| Yasunori Okada, MD, PhD,* and Sachio Kuribayashi, MD, PhD†*

Objectives: To compare the diagnostic performance of computed tomographic (CT) attenuation and CT attenuation ratio at different tube voltages for ex vivo plaque characterization.

Materials and Methods: Human coronary arteries were obtained at the time of autopsy in 15 subjects. The coronary arteries were serially cut into 5-mm-long segments and scanned ex vivo using 4 sets of tube voltages and tube currents (80 kV, 660 mA; 100 kV, 500 mA; 120 kV, 400 mA; and 140 kV, 340 mA). The CT attenuation value at the center of each plaque was obtained, and the ratio of the CT attenuation value at the 80-kV setting divided by that at the 140-kV setting (Hounsfield ratio [HR], 80:140) was calculated. Separate receiver operating characteristic (ROC) analyses were used to assess the usefulness of the CT attenuation value and the 80:140 HR for the differential diagnosis of lipid-rich plaques from other types of plaques.

Results: A total of 93 coronary plaques were detected macroscopically. Histological examination revealed 39 lipid-rich, 24 calcified, and 30 fibrotic plaques. At all the tube voltages, the CT attenuation values of the lipid-rich plaques were lower than those of the calcified plaques, whereas the CT attenuation values of the lipid-rich and fibrotic plaques overlapped. An ROC analysis showed that the area under the curve (AUC) for the differential diagnosis of lipid-rich plaques from fibrotic plaques was 0.813 at 80 kV, 0.772 at 100 kV, 0.682 at 120 kV, or 0.651 at 140 kV. Regarding the 80:140 HR, the AUC was 0.952 (0.029). The AUC was significantly larger at 80 and 100 kV and 80:140 HR compared with the AUC at 120 kV.

Conclusions: The diagnostic performance of CT analysis for ex vivo plaque characterization was superior at lower energy settings and using the dual-energy method.

Key Words: atherosclerosis, computed tomography, radiation exposure

(*J Comput Assist Tomogr* 2010;34: 58–63)

Acute coronary syndromes including unstable angina, acute myocardial infarction, and sudden coronary death are largely attributable to the presence of luminal thrombi superimposed on the rupture of preexisting atherosclerotic plaques.[1,2] In general, lipid-rich plaques are regarded as high-risk lesions that are prone to causing acute coronary syndromes when they progress to lesions with disrupted surfaces, hematomas or hemorrhages, and thrombotic deposits. Inflammatory cells, such as activated macrophages, that are present within atherosclerotic plaques express metalloproteinase enzymes; these enzymes are responsible for the degradation of collagen in fibrous plaques. The result is a weakening of the fibrous cap, leading to the transformation of a lesion from stable to unstable and hence increasing the likelihood of rupture and thrombus. The risks of plaque rupture and subsequent acute coronary syndromes also depend on the composition and structure of atherosclerotic lesions in the coronary arteries.[2] Calcified and fibrotic plaques have a minimal risk of plaque rupture and therefore are regarded as the final stage of the atherosclerotic plaque sequence.[3] Thus, the ability to diagnosis plaque type would provide crucial information regarding the risk of acute coronary syndromes, leading to the establishment of appropriate therapeutic protocols for individual patients.

Noninvasive imaging of the coronary arterial walls has become possible with the introduction of multi–detector row computed tomography (MDCT).[4,5] Although several studies have reported that MDCT for routine clinical diagnosis is capable of detecting coronary plaques and further characterizing their tissue composition,[6–9] the differentiation of lipid-rich plaques from fibrotic plaques is difficult because the CT attenuation values overlap. A number of factors influence plaque density measurements, such as the use of contrast enhancement, partial volume effect, spatial resolution, and motion artifacts. Computed tomographic attenuation values in the same subject also depend on the tube voltages that are used. The measurement of CT attenuation values in a single subject at different energy settings could theoretically provide data that cannot be obtained using a conventional single-energy CT analysis.[10] In general, relatively high voltages, such as 120 or 140 kV, are typically applied for cardiac CT. Recently, cardiac CT protocols using low tube voltages, which enable a reduced radiation dose, have been reported[11,12]; these protocols provided a suitable image quality with a high contrast-to-noise ratio for the detection of plaques. However, the usefulness of CT attenuation with low tube voltages for plaque characterization has not been defined. In this study, we evaluated whether CT attenuation values obtained using different tube voltages were useful for improving plaque differentiation.

MATERIALS AND METHODS

Samples of Coronary Arteries

Human coronary arteries were obtained at the time of autopsy in 15 subjects (11 men and 4 women; mean [SD] age, 72 [9] years). All the coronary arteries were carefully dissected from the heart, and the perivascular adipose tissues were excised. The coronary arteries were serially cut into 5-mm-long segments

From the *Departments of Pathology, and †Radiology, School of Medicine, Keio University, Tokyo; ‡Department of Pathology, Yamaguchi University Graduate School of Medicine, Ube, Yamaguchi; §Preventive Medicine and Public Health; and ||Cardiovascular Laboratory, School of Medicine, Keio University, Tokyo, Japan.
Received for publication March 17, 2009; accepted July 7, 2009.
Reprints: Eiji Ikeda, MD, PhD, Department of Pathology, Yamaguchi University Graduate School of Medicine, 1-1-1 Minami-Kogushi, Ube, Yamaguchi 755-8505, Japan (e-mail: ikedae@yamaguchi-u.ac.jp).

from the coronary ostia until the point where the diameter became 2 mm. All the samples were carefully examined, and the samples with atheromatous plaques (>1 mm in thickness) were selected macroscopically. Finally, 93 plaques were processed for further studies. All the specimens were stored in saline at 4°C until MDCT. Before imaging, the specimens were immobilized in 2-mL Eppendorf tubes containing ultrasonic gel (Logiqlean Hard Type; Kao Corporation, Tokyo, Japan) and were centrifuged at 6,000 rpm for 5 to 20 seconds to remove microbubbles.

The institutional ethical committee at the School of Medicine, Keio University, approved the study protocol, and the family of each subject gave their informed consent for this study.

Multi–Detector Row CT Protocol

Multi–detector row CT data were acquired using the LightSpeed VCT MDCT scanner (GE Healthcare, Milwaukee, WI). First, the CT scanner was calibrated using air phantoms. Ex vivo coronary arteries were oriented parallel to the axis of the gantry. No contrast agent was used. The axial scanning protocol consisted of a gantry rotation period of 2 seconds, a collimation of 32 × 0.625 mm, a matrix size of 512 × 512 pixels, and a field of view of 96 mm. To standardize the signal-to-noise ratio and compensate for the lower photon output at lower voltages, 4 sets of tube voltages and tube currents (80 kV, 660 mA; 100 kV, 500 mA; 120 kV, 400 mA; and 140 kV, 340 mA) were applied. Transverse images were reconstructed using a standard convolution kernel with a 0.625-mm section thickness. The pixel size was 0.19 × 0.19 mm.

To evaluate the image noise in this study, an Eppendorf tube filled with either distilled water, ultrasonic gel, or air was scanned using the same MDCT protocol as described previously, and the CT attenuation was measured using a circular region of interest (area, 10 mm^2) placed in the center of the field of view.

Histological Examination

Immediately after MDCT, the specimens were immersion-fixed with 10% neutral-buffered formalin for histological examination. The specimens were then decalcified in a formic acid for 48 hours and embedded in paraffin. Serial sections (4 μm thick) were stained with hematoxylin-eosin and Elastica van Gieson to identify lipid deposits, calcification, and fibrosis. Two sets of hematoxylin-eosin– and Elastica van Gieson–stained serial sections were prepared from each specimen at an interval of 625 μm. Certified pathologists who were unaware of the results of the MDCT analyses classified the plaques based mainly on the American Heart Association classification.[3] Plaques containing a lipid core with cholesterol crystals and foamy macrophages surrounded by fibrous connective tissue were classified as lipid-rich plaques, whereas those with a significant amount of calcium were classified as calcified plaques, and those with minimal lipid contents or calcification were classified as fibrotic plaques; these categories correspond to the World Health Organization classifications of types IV and Va lesions, type Vb lesions, and type Vc lesions, respectively. Finally, the 93 plaques used in this study were classified as 39 lipid-rich plaques (42%), 24 calcified plaques (26%), and 30 fibrotic plaques (32%).

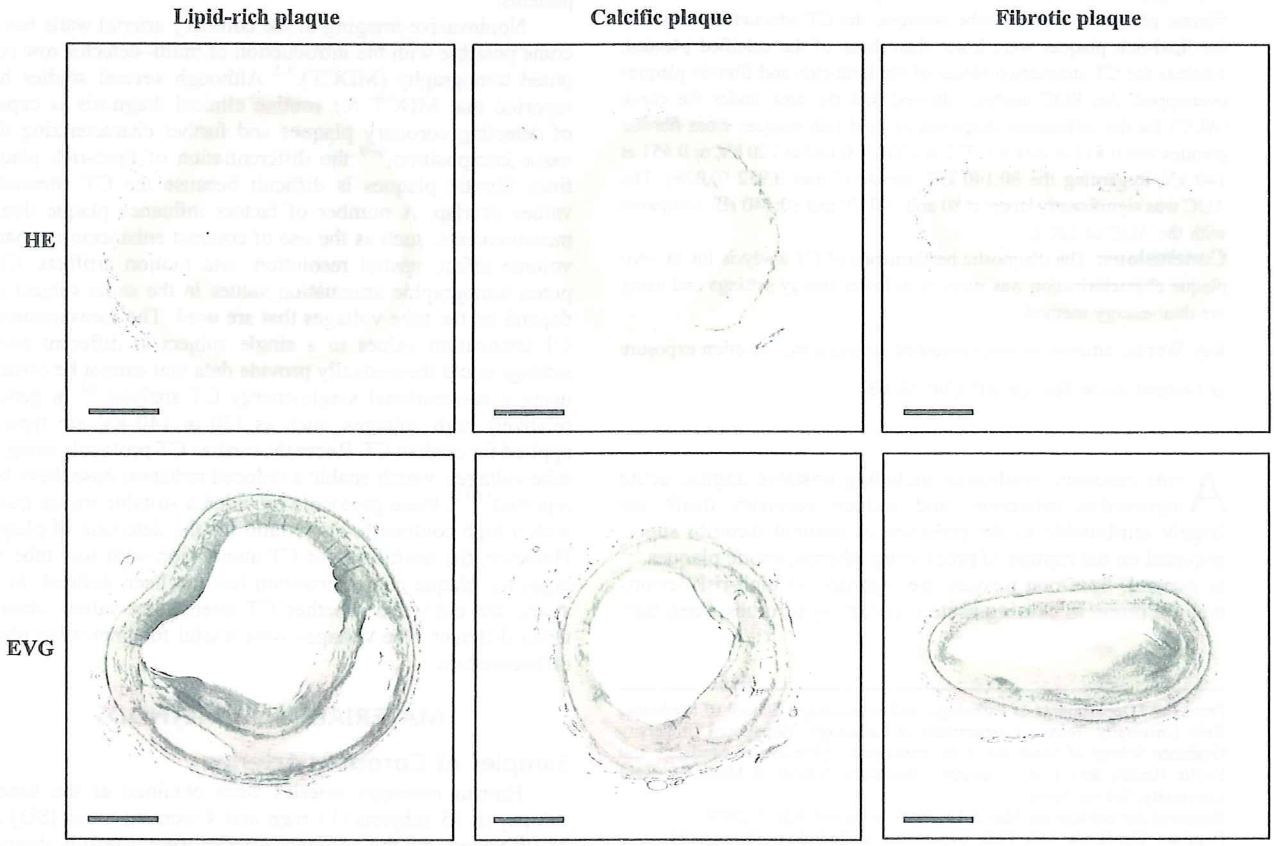

FIGURE 1. Representative histological photographs of lipid-rich, calcified, and fibrotic plaques. HE, hematoxylin-eosin stain; EVG, Elastica van Gieson stain. Bars, 1 mm.

TABLE 1. Computed Tomographic Attenuation Value and 80:140 HR of Each Plaque

	Lipid-Rich Plaque	Calcific Plaque	Fibrotic Plaque
CT attenuation value, kV			
80	20.6 (6.5)	1023 (755)	28.1 (4.3)
100	21.8 (7.3)	882 (650)	27.8 (4.7)
120	23.1 (7.2)	780 (574)	27.1 (5.0)
140	23.9 (7.2)	709 (521)	27.3 (5.1)
80:140 HR	0.86 (0.07)	1.43 (0.07)	1.04 (0.06)

The 80:140 HR is the ratio of CT attenuation value at 80 kV to that at 140 kV.

Each value indicates the mean (SD).

Calculation of CT Attenuation Values and Hounsfield Ratios

Multi-detector row CT data were transferred to a standalone Windows (Microsoft, Redmond, WA) workstation in a Digital Imaging and Communications in Medicine format. A region of interest (5 × 5 pixels; area, 0.9 mm^2) was placed at the center of the plaque, and the CT attenuation value within this region was measured at each voltage. The CT attenuation value of the plaque was calculated as the mean of the attenuation values measured for a pixel-sized area within the square region. Furthermore, the ratio of the CT attenuation value at the lower kV setting to that at the higher kV setting was calculated for each pixel-sized area, and the mean within the region was defined as the Hounsfield ratio (HR) of the plaque. For example, the ratio of the CT attenuation value at the 80-kV setting to that at the 140-kV setting was defined as 80:140 of the plaque.

Assessment of Plaque Characterization

The accuracy of classifying lipid-rich and fibrotic plaques was assessed. If a sample was above the threshold, the plaque was considered to be fibrotic; if a sample was below the threshold, the plaque was considered to be lipid-rich.

Statistical Analysis

The usefulness of the CT attenuation value and the 80:140 HR for the differential diagnosis of lipid-rich and fibrotic plaques was assessed using a receiver operating characteristic (ROC) analysis. The ROC analysis was performed using a software package (Stata, version 9.1; StataCorp, College Station, Tex) to calculate the area under the curve (AUC) and the SE. Differences in the AUC values between the groups relative

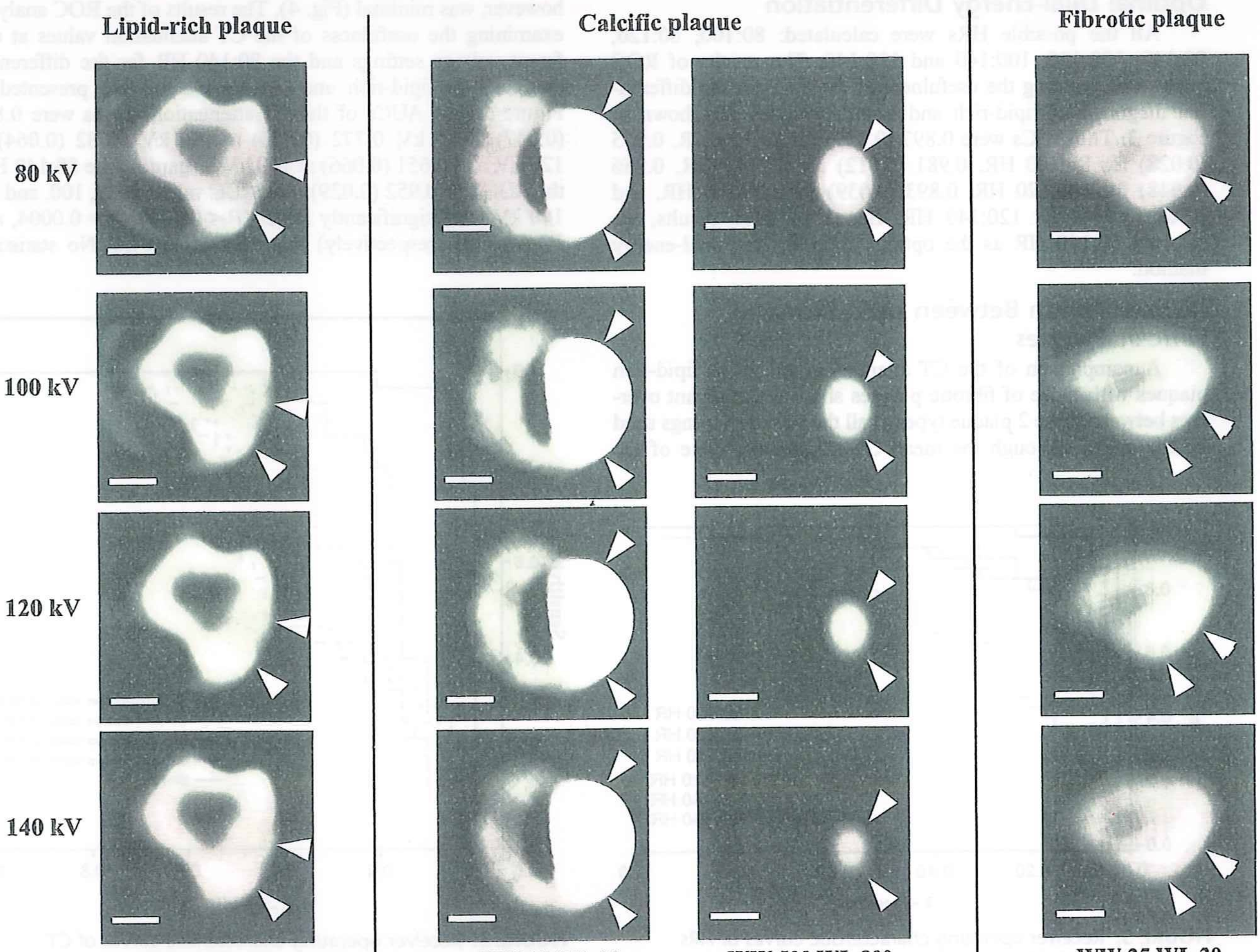

FIGURE 2. Computed tomographic images of coronary arteries at different energy settings. Computed tomographic images of the coronary arteries shown in Figure 1 are presented, and the areas of the plaques are indicated by the arrowheads. Bars, 1 mm.

to the AUC at 120 kV, which our institution uses as a standard, were statistically examined using the AUC, and the areas under correlated ROC curves were analyzed using the nonparametric approach described by DeLong et al[13] with a Bonferroni correction for multiple comparisons. $P < 0.05$ was considered statistically significant.

RESULTS

Histological Classification and CT Images of Coronary Arteries

A total of 364 coronary artery segments were investigated, revealing 93 plaques (39 lipid-rich, 24 calcified, and 30 fibrotic plaques) with more than 1 mm in thickness; these segments were processed for further studies. Representative histological photographs are presented in Figure 1. Using the MDCT protocol in this study, the mean (SD) CT attenuation values and image noise of water were 2.0 (1.0) Hounsfield units (HU) at 80 kV, 0.3 (1.1) HU at 100 kV, −1.2 (1.0) HU at 120 kV, and −1.8 (1.0) HU at 140 kV. All the coronary artery samples were successfully placed in the center of the gantry, and their CT attenuation values were measured at 80, 100, 120, and 140 kV; the HRs were then calculated (Table 1). Computed tomographic images of a single sample obtained at different energy settings are shown in Figure 2.

Optimal Dual-Energy Differentiation

All the possible HRs were calculated: 80:100, 80:120, 80:140, 100:120, 100:140 and 120:140. The results of ROC analyses examining the usefulness of the HRs for the differential diagnosis of lipid-rich and fibrotic plaques are shown in Figure 3. The AUCs were 0.897 (0.039) for 80:100 HR, 0.955 (0.028) for 80:120 HR, 0.981 (0.012) for 80:140 HR, 0.856 (0.048) for 100:120 HR, 0.893 (0.039) for 100:140 HR, and 0.701 (0.064) for 120:140 HR. Based on these results, we selected 80:140 HR as the optimal ratio for the dual-energy method.

Differentiation Between Lipid-Rich and Fibrotic Plaques

A comparison of the CT attenuation values of lipid-rich plaques with those of fibrotic plaques showed significant overlaps between these 2 plaque types at all the voltage settings used in this study, although the mean CT attenuation value of the

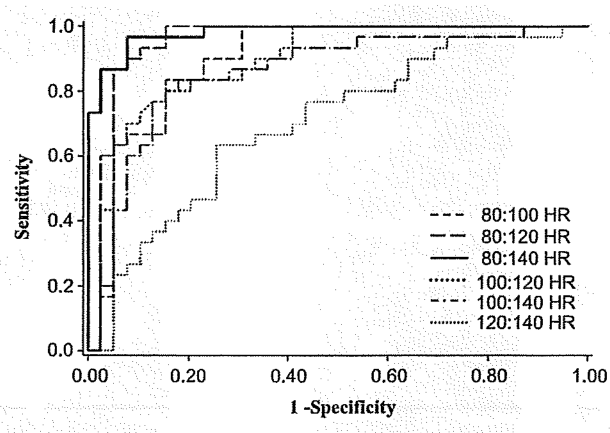

FIGURE 3. Receiver operating characteristic curves of HRs (at settings of 80:100, 80:120, 80:140, 100:120, 100:140, and 120:140 HRs) for evaluating the diagnostic performance of these parameters for differentiating lipid-rich and fibrotic plaques.

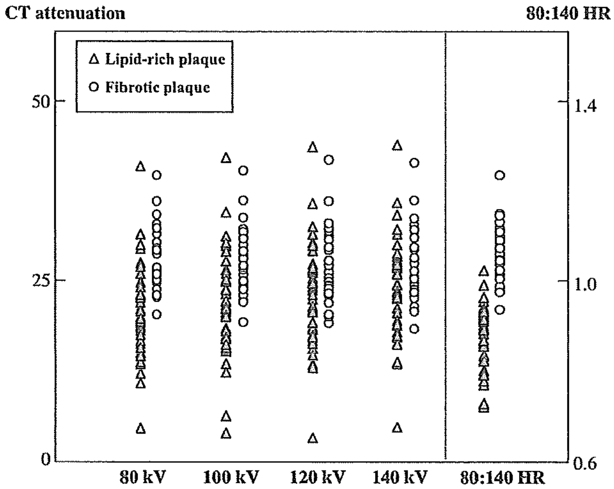

FIGURE 4. Comparison of CT attenuation values (at settings of 80, 100, 120, and 140 kV) and 80:140 HR for lipid-rich (▲) and fibrotic plaques (○).

lipid-rich plaques was lower than that of the fibrotic plaques (Fig. 4). The overlap of the 80:140 HRs of these 2 plaque types, however, was minimal (Fig. 4). The results of the ROC analyses examining the usefulness of the CT attenuation values at different voltage settings and the 80:140 HR for the differential diagnosis of lipid-rich and fibrotic plaques are presented in Figure 5. The AUCs of the CT attenuation values were 0.813 (0.047) at 80 kV, 0.772 (0.056) at 100 kV, 0.682 (0.064) at 120 kV, and 0.651 (0.066) at 140 kV. Regarding the 80:140 HR, the AUC was 0.952 (0.029). The AUC values at 80, 100, and 80/140 kV were significantly larger ($P < 0.0001$, $P = 0.0004$, and $P < 0.0001$, respectively) than that at 120 kV. No statistical

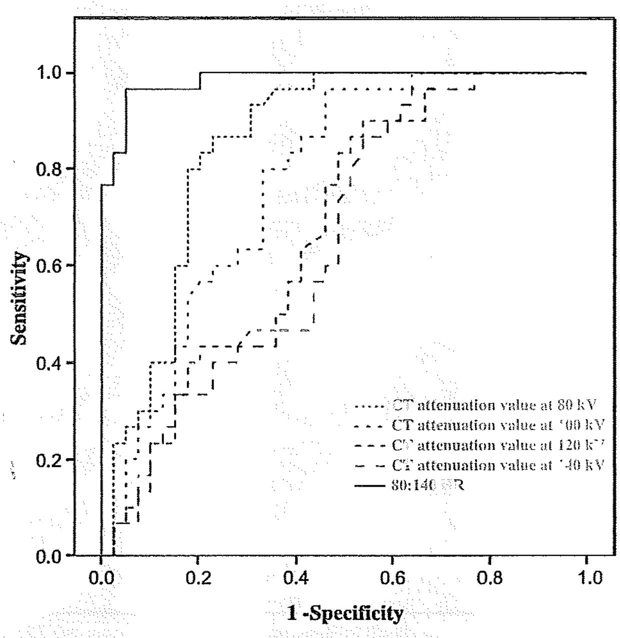

FIGURE 5. Receiver operating characteristic curves of CT attenuation values (at settings of 80, 100, 120, and 140 kV) and 80:140 HR for evaluating the diagnostic performance of these parameters for differentiating lipid-rich and fibrotic plaques.

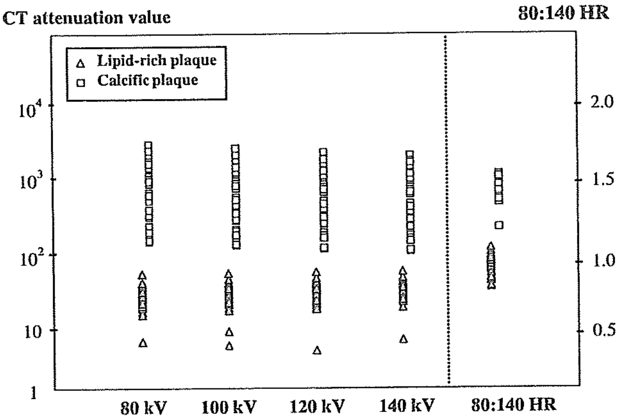

FIGURE 6. Comparison of CT attenuation values (at settings of 80, 100, 120, and 140 kV) and 80:140 HR for lipid-rich (▲) and calcified plaques (□). No overlap in the CT attenuation values or the 80:140 HRs was observed between these 2 plaque types.

difference between the AUC at 120 kV and that at 140 kV was seen ($P = 0.17$).

Differentiation of Lipid-Rich and Calcified Plaques

For a given tube voltage, the maximum CT attenuation value of the lipid-rich plaques was distinctly lower than the minimum CT attenuation value of the calcified plaques (Fig. 6). In addition, the 80:140 HRs of the 2 plaque types did not overlap, with an AUC of 1.0. No statistically significant difference in the differentiation accuracy of the CT attenuation value and the 80:140 HR ratio was seen.

Radiation Dose at Each Voltage

The doses according to the CT dose index volume (CTDIv) were 38.3 mGy at 80 kV, 47.6 mGy at 100 kV, 64.5 mGy at 120 kV, and 76.7 mGy at 140 kV. The CTDIv using the 80:140 HR method was 115 mGy. Although the image noise was almost the same, the CTDIv at 80 kV was the smallest of the various voltages that were used.

DISCUSSION

The establishment of a diagnostic protocol for differentiating lipid-rich plaques from calcified or fibrotic plaques is essential for the application of appropriate therapeutic strategies in patients with coronary atherosclerosis. Several studies have reported that cardiac CT is capable of detecting coronary plaques and further characterizing their tissue composition.[6–9] Our study showed that the CT attenuation values at any of several energy settings showed no overlap between lipid-rich and calcified plaques. These data demonstrated that the measurement of CT attenuation values at a single-energy setting is sufficient to enable a distinction between these 2 types of plaques and support the findings of previous studies showing that the differentiation of lipid-rich and calcified plaques can be achieved by measuring the CT attenuation value at a single-energy setting.[6–9] Regarding the differential diagnosis of lipid-rich plaques from other types of plaques, the AUC obtained at 80 kV was higher than those obtained at any other tube voltage. Furthermore, when the voltage was set at 80 kV, the CTDIv, an index of radiation exposure, was lower than that obtained at any other voltage setting. The recent increase in radiation exposure from CT has become a worldwide problem, and efforts to reduce the radiation doses delivered during CT examinations are an important issue.[14] Some studies have reported that the radiation dose itself can be reduced by lowering the tube voltage of the CT examination.[11,12] In the present study, we applied a tube voltage of 80 kV for cardiac CT, which is usually performed at a setting of 120 kV, to determine whether imaging at 80 kV could improve plaque characterization without increasing the radiation dose. Our data showed that a CT examination performed at 80 kV provided a CT attenuation value with a significantly higher diagnostic performance for identifying lipid-rich plaques, compared with the results obtained at the other voltage settings used in the present study.

Although the diagnostic performance at the 80-kV setting was the best among the single-energy settings, CT attenuation values for lipid-rich and fibrotic plaques overlapped. Therefore, we evaluated a dual-energy CT analysis for the differential diagnosis of lipid-rich plaques, especially from fibrotic plaques. Using dual-energy CT, Clasen et al[15] calculated the HR, which was defined as the reading in absolute units at the 100-kV setting divided by that at the 140-kV setting. They concluded that an exponential relationship existed between the effective atomic number and the HR of the substances. Although most in vivo tissues are composed of elements with nearly the same effective atomic numbers as water,[16] certain materials contain elements with effective atomic numbers distinct from that of water. Accordingly, some investigators have proposed the possibility of using dual-energy CT for the diagnosis of fatty liver[17] or lipid-containing tumors[18] and the analysis of bone mineral density.[19] In atheromatous plaques, the lipid core consists mainly of cholesterol esters,[20] with an effective atomic number that is lower than that of water; on the other hand, calcifications consist of hydroxyapatite,[21] which is also a major component of cortical bone, and have an effective atomic number that is higher than that of water. These plaque characteristics led us to propose that a comparison of the CT attenuation value at a low energy setting with that at a high energy setting might enable the differential diagnosis of lipid-rich plaques from other types of plaques.

In this study, the CT attenuation value obtained at the 80-kV setting was divided by that obtained at the 140-kV setting to give the 80:140 HR. According to our results, the mean (SD) 80:140 HRs of the lipid-rich plaques and the fibrotic plaques were 0.86 (0.07) and 1.04 (0.06), respectively. An ROC analysis revealed that the AUC of the 80:140 HR for the differential diagnosis between these 2 types of plaques was significantly better than that of the CT attenuation value at any single-energy setting, and the high AUC of the 80:140 HR (0.985 [0.011]) means that lipid-rich plaques could be discriminated from fibrotic plaques with an excellent diagnostic performance. However, the radiation dose delivered by the 80:140 HR method is higher than that delivered using the single-energy CT attenuation method. Thus, further studies are needed to determine whether the improvement in plaque characterization using the 80:140 HR method justifies the increase in radiation exposure.

The present study had some limitations. First, the slice thickness used for the histological evaluation (4 μm) was different from that of the MDCT analysis (625 μm). Even in the latest CT scanner, the spatial resolution is not sufficient to assess the tissue composition within a coronary plaque; thus, higher resolution CT is eagerly awaited. Second, despite the small pixel size and slice thickness used in the present study, the image noise was relatively small. In a clinical situation, however, the image noise might be affected by patient size and motion artifacts caused by the heartbeat. Moreover, the scanner used in the present study exhibits a higher noise level at lower kV settings in large patients. Thus, a higher intracoronary attenuation may be required to compensate for the lower image noise. These problems must be solved before the present results can be applied to routine clinical examinations.

CONCLUSIONS

In this ex vivo study, the diagnostic performance of CT analysis for plaque characterization was significantly better at lower energy settings (80 and 100 kV) and using the dual-energy method (80:140 HR) compared with that at 120 kV. However, further evaluations are needed to determine whether these results are applicable for clinical use.

REFERENCES

1. Kolodgie FD, Virmani R, Burke AP, et al. Pathologic assessment of the vulnerable human coronary plaque. *Heart*. 2004;90:1385–1391.
2. Libby P. Current concepts of the pathogenesis of the acute coronary syndromes. *Circulation*. 2001;104:365–372.
3. Stary HC. Natural history and histological classification of atherosclerotic lesions: an update. *Arterioscler Thromb Vasc Biol*. 2000;20:1177–1178.
4. Hoffmann MH, Shi H, Schmitz BL, et al. Noninvasive coronary angiography with multislice computed tomography. *JAMA*. 2005;293:2471–2478.
5. Nieman K, Cademartiri F, Lemos PA, et al. Reliable noninvasive coronary angiography with fast submillimeter multislice spiral computed tomography. *Circulation*. 2002;106:2051–2054.
6. Pohle K, Achenbach S, Macneill B, et al. Characterization of non-calcified coronary atherosclerotic plaque by multi–detector row CT: comparison to IVUS. *Atherosclerosis*. 2007;190:174–180.
7. Rasouli ML, Shavelle DM, French WJ, et al. Assessment of coronary plaque morphology by contrast-enhanced computed tomographic angiography: comparison with intravascular ultrasound. *Coron Artery Dis*. 2006;17:359–364.
8. Carrascosa PM, Capunay CM, Garcia-Merletti P, et al. Characterization of coronary atherosclerotic plaques by multidetector computed tomography. *Am J Cardiol*. 2006;97:598–602.
9. Schroeder S, Kuettner A, Wojak T, et al. Non-invasive evaluation of atherosclerosis with contrast enhanced 16 slice spiral computed tomography: results of ex vivo investigations. *Heart*. 2004;90:1471–1475.
10. Kalender WA, Perman WH, Vetter JR, et al. Evaluation of a prototype dual-energy computed tomographic apparatus. I. Phantom studies. *Med Phys*. 1986;13:334–339.
11. Sigal-Cinqualbre AB, Hennequin R, Abada HT, et al. Low-kilovoltage multi–detector row chest CT in adults: feasibility and effect on image quality and iodine dose. *Radiology*. 2004;231:169–174.
12. Heyer CM, Mohr PS, Lemburg SP, et al. Image quality and radiation exposure at pulmonary CT angiography with 100- or 120-kVp protocol: prospective randomized study. *Radiology*. 2007;245:577–583.
13. DeLong ER, DeLong DM, Clarke-Pearson DL. Comparing the areas under two or more correlated receiver operating characteristic curves: a nonparametric approach. *Biometrics*. 1988;44:837–845.
14. Paul JF, Abada HT. Strategies for reduction of radiation dose in cardiac multislice CT. *Eur Radiol*. 2007;17:2028–2037.
15. Clasen RA, Rayudu GV, Pandolfi S, et al. Dual energy computerized tomography: a simplified approach. *Comput Radiol*. 1983;7:261–266.
16. Yang NC, Leichner PK, Hawkins WG. Effective atomic numbers for low-energy total photon interactions in human tissues. *Med Phys*. 1987;14:759–766.
17. Wang B, Gao Z, Zou Q, et al. Quantitative diagnosis of fatty liver with dual-energy CT. An experimental study in rabbits. *Acta Radiol*. 2003;44:92–97.
18. Raptopoulos V, Karellas A, Bernstein J, et al. Value of dual-energy CT in differentiating focal fatty infiltration of the liver from low-density masses. *AJR Am J Roentgenol*. 1991;157:721–725.
19. Kalender W, Bautz W, Felsenberg D, et al. Material-selective imaging and density measurement using the dual-energy method. I. Principles and methodology [in German]. *Digitale Bilddiagn*. 1987;7:66–72.
20. Oliver MF, Davies MJ. The atheromatous lipid core. *Eur Heart J*. 1998;19:16–18.
21. Doherty TM, Asotra K, Fitzpatrick LA, et al. Calcification in atherosclerosis: bone biology and chronic inflammation at the arterial crossroads. *Proc Natl Acad Sci U S A*. 2003;100:11201–11206.

Extracardiac structures are frequently present within close proximity to the left atrium: Relevance to catheter ablation

Seiji Takatsuki, MD,* Minoru Yamada,† Kotaro Fukumoto, MD,* Kojiro Tanimoto, MD,* Masahiro Jinzaki, MD,† Sachio Kuribayashi, MD,† Satoshi Ogawa, MD*

*From the *Cardiology Department, Keio University School of Medicine, Tokyo, Japan, and the †Radiology Department, Keio University School of Medicine, Tokyo, Japan.*

BACKGROUND The coronary sinus (CS) including the great cardiac vein is an important anatomic structure that is considered a landmark for the mitral annulus (MA) and also a target for catheter ablation.

OBJECTIVE This study evaluated the anatomical relationship between the CS and its surrounding structures visualized by multidetector computed tomography (MDCT).

METHODS We performed MDCT on 42 patients, and the ranges of the coronary arteries (CAs) and esophagus that ran closest (<5 mm) to the CS were examined. In addition, the distances between the CS and the MA and left ventricle and left atrium were compared with the amplitudes of the local atrial and ventricular electrograms in the CS at the most lateral point (3 o'clock) and the inferior point (6 o'clock) in the CS.

RESULTS The distal portion of the right CA ran near the anteroinferior side of the CS ostium in 92% of the patients. The esophagus and the left circumflex CA proximity to the CS ran from 15 to 41 mm and from 53 to 104 mm from the ostium in all patients. At the 3 o'clock and 6 o'clock position of the MA, the distance between the center of the CS and MA was 12 and 13 mm, respectively, and showed negative correlation with the ratio of atrial and ventricular electrograms.

CONCLUSION The right CA, the left circumflex CA, and the esophagus were frequently located near the CS. The CS was shifted away from the MA, and the CS–MA distance could be predicted with intracardiac electrograms.

KEYWORDS Coronary sinus; Computed tomography; Catheter ablation; Coronary artery; Esophagus.

ABBREVIATIONS 3D = 3-dimensional; **Aamp** = amplitude of the atrial potential; **CA** = coronary artery; **CPR** = curved planar reconstruction; **CS** = coronary sinus; **CT** = computed tomography; **LA** = left atrium; **LV** = left ventricle; **MA** = mitral annulus; **MDCT** = multidetector computed tomography; **Vamp** = amplitude of the ventricular potential.

(Heart Rhythm 2009;6:1559–1564)

Introduction

In the fields of catheter ablation and clinical electrophysiology, the coronary sinus (CS), including the great cardiac vein, plays an important role in the cardiac apparatus. An electrode catheter is routinely placed into the CS to be used as a stable atrial pacing site and to provide for an anatomical marker for the mitral annulus during an electrophysiologic study. Moreover, the muscular sleeve around the CS or the myocardium near the CS can be a target for catheter ablation therapy. Radiofrequency application from inside the CS might be needed to cure tachyarrhythmias, such as atrioventricular nodal reentrant tachycardia,[1] atrioventricular reciprocating tachycardia,[2–4] atrial tachycardia,[5,6] atrial fibrillation,[7] and idiopathic ventricular tachycardia.[8] It has also been reported that radiofrequency application inside the CS can be an effective strategy to make a conduction block in the lateral mitral isthmus for the curative treatment of atrial fibrillation.[9,10] Although rare, such radiofrequency application inside the CS has the potential for serious complications.[11] Therefore, it is considered essential for electrophysiologists to have an understanding of the anatomy of the CS and its surrounding structures.

Recent advancements in cardiac image technology, especially multidetector computed tomography (MDCT) capabilities of high spatial resolution, have allowed for precise, noninvasive 3-dimensional (3D) imagining and delineation of the cardiac anatomy. It has also proven to be a valuable tool to provide an analysis of the cardiac venous system.[12,13] This study was conducted to clarify the anatomical relationship between the CS and its surrounding structures (i.e., coronary arteries, esophagus, and mitral annulus [MA]) using 3D MDCT imaging, and also to identify any correlating characteristics between the electrograms recorded inside the CS in relation to the distance between the CS and the MA as visualized by MDCT.

The authors thank Jeffrey Annis for his linguistic advice. **Address reprint requests and correspondence:** Dr. Seiji Takatsuki, Cardiology Department, Keio University School of Medicine, 35 Shinanomachi, Shinjukuku, Tokyo 160-8582, Japan. E-mail address: seiji.takatsuki@gmail.com. (Received April 29, 2009; accepted July 28, 2009.)

1547-5271/$ -see front matter doi:10.1016/j.hrthm.2009.07.049

Methods

Study population

This study consisted of 42 patients (40 men, 56 ± 10 years old) who underwent cardiac MDCT before catheter ablation for the treatment of paroxysmal atrial fibrillation. No patients had structural heart diseases. The procedures were in accordance with institutional guidelines, and all patients gave informed consent before the conduction of cardiac computed tomography (CT) and the electrophysiologic study.

MDCT data acquisition

An electrocardiogram-gated helical CT scan of the heart was performed within 1 week before the ablation procedure. Images were acquired with a LightSpeed 16, 16-row multidetector CT scanner, or LightSpeed VCT, 64-row multidetector CT scanner (GE Healthcare, Milwaukee, Wisconsin). Scanning of the entire heart was performed within a single breath-hold, with 16 or 64 × 0.625 mm collimation. The gantry rotation time was 0.35 to 0.5 seconds, and the pitch was between 0.20 and 0.24. The tube current was 350 to 750 mA at 120 kV. Iodine contrast material (40 to 60 ml; Iopamidol 370 mg/ml, Schering, Berlin, Germany), followed by 20 ml of saline, was injected at a rate of 3 to 4 ml/s. The axial images of every 75% in the cardiac phase were reconstructed with a resolution of 512 × 512 matrix. The reconstructed data were transferred to the workstation system (Advantage Workstation version 4.2, GE Healthcare) for further processing.

Data analysis

In all patients, the CS, the right coronary artery (CA), the left circumflex CA, and the left cardiac cavity were reconstructed as a complete 3D image using images taken as maximal intensified projections that were compiled and formatted on a QuickTime multimedia framework providing 360° views from all directions (Figure 1). A stretched curved planar reconstruction (CPR) image and a cross-sectional image of the CS were then semi-automatically reconstructed on the workstation. When the central axis of the stretched CPR did not automatically align itself to the center of the CS lumen, the correction was manually performed by an image-processing specialist (M.Y.) from images taken from the multiplanar reconstruction. The longer and shorter diameters of CS and the distance from the CS to the right CA (from edge to edge), esophagus, and left circumflex CA were then measured on the cross-sectional images (Figure 2). Structures that were considered proximate to any region along the CS (distance <5 mm) were further investigated, and their distances from the CS ostium were measured.

CS and mitral annulus with electrophysiological analysis

In 30 of 42 patients, intracardiac electrograms were obtained by a 6F 14-polar catheter placed inside the CS (Irvine Medical, Irvine, California). The CS electrograms were taken during sinus rhythm before ablation and stored and analyzed on a computer-based digital amplifier/recorder system (CardioLab, Prucka-GE, Houston, Texas). Intracardiac electrograms were filtered from 30 to 500 Hz and measured using online calipers at a sweep speed of 100 mm/s. The amplitudes of the atrial potential (Aamp) and the ventricular potentials (Vamp) were measured at the most lateral point and the most inferior point within the CS electrodes, i.e., in the direction of 3 o'clock and 6 o'clock in

Figure 1 Three-dimensionally reconstructed CS (blue), the right CA (yellow), the left CA (red), and the left heart. CA = coronary artery; CS = coronary sinus.

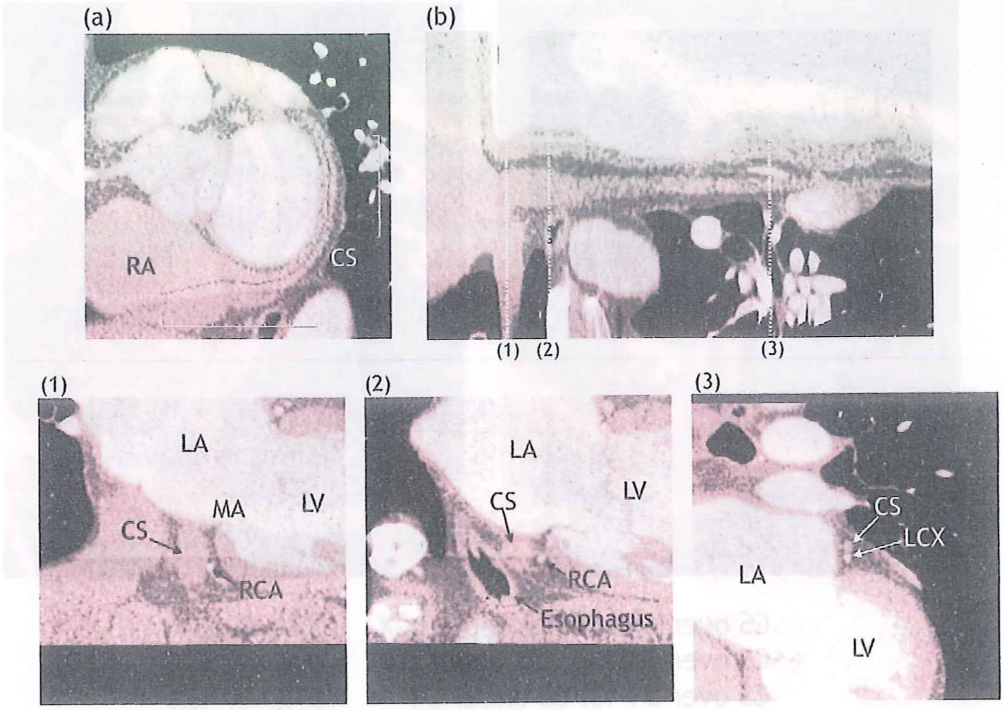

Figure 2 **a:** CS shown with multiplanar reconstruction. **b:** CS shown with stretched curved planar reconstruction. **1:** Cross-sectional image of CS at the ostium. Ostium of the CS and the distal part of the right coronary artery (RCA) are shown. **2:** Cross-sectional image of CS at 10 mm from the ostium. The RCA and the esophagus attaching the CS are shown. **3:** Cross-sectional image of the CS at 60 mm from the ostium. The left circumflex coronary artery (LCX) is shown. CA = coronary artery; CS = coronary sinus; LA = left atrium; LV = left ventricle; MA = mitral annulus; RA = right atrium.

the left anterior oblique view. The distances between the center of CS and MA (CS–MA distance) and from the edge of the CS to MA, the nearest left atrial wall to the CS (CS–LA distance), and the nearest left ventricular wall to the CS (CS–LV distance) were also measured on the 3-dimensional CT at the most lateral point and the most inferior point of the CS. The relationships between the Aamp and the CS–LA distance, the Vamp and the CS–LV distance, the ratio of the Aamp over Vamp (A/V ratio), and the CS–MA distance were investigated.

Statistical analysis

Parametric data are expressed as mean ± standard deviation. The relationships between the Aamp and the CS–LA distance, the Vamp, and the CS–LV distance were analyzed with the exponential regression test. The relationship between the A/V ratio and the CS–MA distance was analyzed with the simple regression test. A P value $<.05$ was considered to be statistically significant.

Results

CS and surrounding anatomical structures

Forty patients had the right dominant system of CA, and 2 patients had the left dominant system. The diameter of the coronary sinus ostium was 19 ± 4 mm × 11 ± 4 mm. The distal portion of the right CA ran near (<5 mm) the antero-inferior side of the CS ostium in 92% (37 of 40) of the patients having a right dominant system, with the average distance being 2.9 ± 2.5 mm. The position of the distal right CA around the CS ostium was distributed in 2 patients in the direction from 3 o'clock to 3:30, 9 patients from 4 o'clock to 4:30, 21 patients from 5 o'clock to 5:30, and 9 patients from 6 o'clock to 6:30. The right CA traveled along the CS up to 17 ± 8 mm from the CS ostium (Figure 3). The esophagus ran near (<5 mm) the CS from 15 ± 8 mm to 41 ± 11 mm from the CS ostium in the posterior direction in all patients.

The left circumflex CA traveled near (<5 mm) the CS in all patients from 53 ± 34 to 104 ± 14 mm from the ostium. In 40 patients who had the right dominant CA system, the left circumflex CA crossed the CS in 2 patients in the direction from 12 o'clock to 12:30 of the mitral annulus

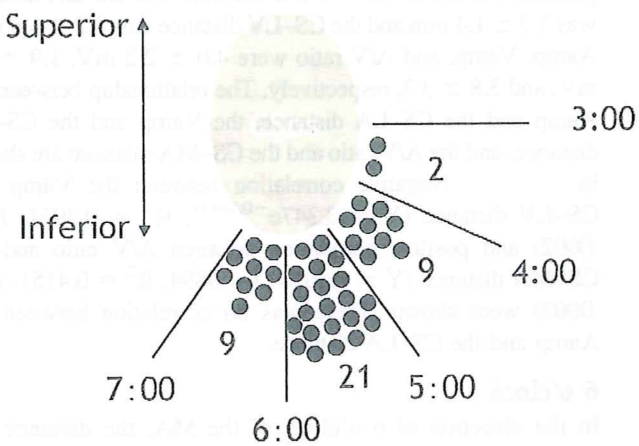

Figure 3 Position of the distal right coronary at the coronary sinus ostium.